SCIENCE CHINA
Technological Sciences

•Article•

February 2020 Vol.63 No.2: 303–318
https://doi.org/10.1007/s11431-018-9469-9

A new method of developing elastic-plastic-viscous constitutive model for clays

LU DeChun, MIAO JinBo, DU XiuLi* & LIANG JingYu

Key Laboratory of Urban Security and Disaster Engineering of Ministry of Education, Beijing University of Technology, Beijing 100124, China

Received November 19, 2018; accepted February 22, 2019; published online May 15, 2019

A new method is presented to develop the existing elastic-plastic constitutive model into an elastic-plastic-viscous one for clays. The actual loading process is divided into an instant process and a delayed process denoting the elastic-plastic strain and viscous strain, respectively. The elastic-plastic strain is determined by either an elastic-plastic model for overconsolidated clays or an improved model based on the elastic-plastic model for normally consolidated clays. In order to calculate viscous strain, a reference state line is defined based on the actual loading path. Combining the reference state line, an existing elastic-plastic model can be conveniently developed into an elastic-plastic-viscous model. Furthermore, using the proposed method, the modified cam clay model is extended into an elastic-plastic-viscous model. Comparisons with test results demonstrate that the extended model can capture the main time-dependent behaviours of clays, including creep, stress relaxation and strain rate effects.

clays, constitutive model, reference state line, time-dependent behaviours, creep, strain rate

Citation: Lu D C, Miao J B, Du X L, et al. A new method of developing elastic-plastic-viscous constitutive model for clays. Sci China Tech Sci, 2020, 63: 303–318, https://doi.org/10.1007/s11431-018-9469-9

1 Introduction

The deformation of clays is time-dependent. For example, clays will be compressed gradually even under constant pressure, which is called creep. If the deformation of clays is constrained, the applied stress becomes lower and lower as time goes on, which is called stress-relaxation. Many time-dependent constitutive models describing the stress-strain-time relationship of clays have been proposed. These models can be generally divided into three categories [1,2]: empirical models, rheological models and general stress-strain-time (GSST) models. Empirical models [3–5] are specific type of mathematical expressions that are fitted through experimental results. They capture the principal behaviours of clays in a simple manner, but their application is limited to test conditions similar to those that they were constructed for [1,6]. Rheological models [7–9] are combination of mechanical components, such as elastic springs, plastic sliders and viscous dashpots. The models are simple in concept and clear in physical meaning. However, the mechanical components are presented under certain stress conditions, and it is difficult for them to describe the deformation behaviours of clays under complex stress conditions, especially dilatancy. GSST models [10–18] are proposed by introducing delayed deformation into total deformation in the framework of the viscoplastic theory. Thus, GSST models can reasonably describe the time-dependent deformation behaviours under general stress conditions.

GSST models are further classified into two main categories [19,20]: overstress models and non-stationary flow surface (NSFS) models. Overstress models [21,22] are proposed based on Perzyna's overstress theory [23,24]. The

*Corresponding author (email: duxiuli@bjut.edu.cn)

value of the viscous strain increment $d\varepsilon_{ij}^{v}$ is an overstress function described by the distance between dynamic yield surface f_d and static yield surface f_s. Moreover, f_d always passes the current stress state point, and f_s denotes an elastic zone that corresponds to the yield surface of classical plasticity theory. f_s needs to be determined by extremely slow tests [25]. Typically, f_s is replaced by a reference surface f_r [26,27] that is determined by constant strain rate tests. Nevertheless, most overstress models cannot describe the acceleration creep under undrained conditions [20,28,29].

NSFS models [19,30] are further developments of elastic-plastic (EP) models. A time-dependent equation is incorporated into the yield function f to reflect the value of viscous strain increment, and the plastic multiplier contains a stress-dependent part and a time-dependent part. This approach makes the loading-unloading criterion complex, since the criterion is not only dependent on stress increment, but also related to time. Besides, the material is considered to be elastic-viscous-plastic on f and elastic inside f. Therefore, NSFS models can only describe viscoplastic behaviours for normally consolidated clays. The initial stress state of overconsolidated clays is inside f, and thus time effects, such as creep and stress relaxation, cannot be described [1].

On the other hand, new NSFS model based on the concept of reference time line (RTL) is proposed by Yin and Graham [31] and Yin et al. [32]. The RTL is an isotropic compression line at a constant strain rate. The equivalent time is thereby evaluated by referring to the RTL and used to determine the irreversible deformation. Yin et al. [32] introduce the RTL into their own model and obtains good prediction for the time-dependent behaviours of both normally consolidated and overconsolidated clays.

A new method to develop EP models into elastic-plastic-viscous (EPV) models for clays is proposed in this paper. The total deformation is divided into a stress-dependent part and a time-dependent part representing the elastic-plastic and viscous strain increments, respectively. The elastic-plastic strain increment is determined by an EP model. A reference state line (RSL) is defined based on the actual loading path. It is the instant loading line for normally consolidated clays and different from RTL: (1) the loading rate of RSL is infinity; (2) the stress state corresponding to RSL is not limited to isotropic compression conditions, but can be with shear stress. By introducing RSL, the viscous strain increment can be calculated and existing EP models can be developed into EPV models. As an example, the modified cam clay (MCC) model is extended into an EPV model. The new model is validated by oedometer tests and various triaxial compression tests on clays, including constant strain rate tests, step-changed strain rate tests, creep tests and stress relaxation tests.

2 Framework of EPV theory for clays

In the framework of EPV theory for clays, the total strain increment $d\varepsilon_{ij}$ is divided into two parts [33].

$$d\varepsilon_{ij}=d\varepsilon_{ij}^{s}+d\varepsilon_{ij}^{v}, \tag{1}$$

where $d\varepsilon_{ij}^{v}$ is the delayed strain increment, i.e., the viscous strain increment, which is the deformation under action of time when subjected to constant external load; $d\varepsilon_{ij}^{s}$ is the instant strain increment, i.e., the elastic-plastic strain increment, which is only caused by stress changes and independent of time. Furthermore, $d\varepsilon_{ij}^{s}$ is the summation of the elastic strain increment $d\varepsilon_{ij}^{e}$ and the plastic strain increment $d\varepsilon_{ij}^{p}$, which is written as

$$d\varepsilon_{ij}^{s}=d\varepsilon_{ij}^{e}+d\varepsilon_{ij}^{p}. \tag{2}$$

Therefore, the total strain increment is expressed as

$$d\varepsilon_{ij}=d\varepsilon_{ij}^{e}+d\varepsilon_{ij}^{p}+d\varepsilon_{ij}^{v}. \tag{3}$$

The elastic, plastic and viscous strains separately involve clear physical meanings. The elastic and plastic strains simultaneously occur under loading conditions, while only the elastic strain is produced under unloading conditions. The viscous strain always develops with time, regardless of loading or unloading. Thus, the behaviours of clays differ under loading and unloading conditions. The deformation mechanisms of clays are separately explained.

With respect to loading conditions, the deformation of clays is elastic-plastic-viscous. Take an infinitesimal stress path C_nC_{n+1} in Figure 1(a) as an example, and the time duration is dt. Correspondingly, C_nC_{n+1} in the e-ln$p$ plane is shown in Figure 1(b). Here, p is the mean stress, and $p = 1/3\sigma_{ii}$; q is the generalized deviator stress, and $q = \sqrt{3/2 s_{ij}s_{ij}}$, where $s_{ij} = \sigma_{ij} - p\delta_{ij}$; e is the void ratio; and f is the yield curve. In the e-ln$p$ plane, C_nC_{n+1} is divided into an instant process C_nB_{n+1} and a delayed process $B_{n+1}C_{n+1}$. The elastic-plastic strain increment of C_nB_{n+1} depends on the stress path and the overconsolidation state of C_n, and can be determined by existing EP models. The viscous strain increment of $B_{n+1}C_{n+1}$ is related to both dt and the overconsolidation state of point B_{n+1}. The overconsolidation state is typically reflected by the over consolidation ratio (OCR) that describes the distance from the current state of clays to their corresponding normal consolidation state. Additionally, the OCR of C_n (OCR_{C_n}) and $OCR_{B_{n+1}}$ can be determined by the void ratios of A_n and A_{n+1}, respectively. Here, A_n and A_{n+1} are the normal consolidation state points of clay under the same stress conditions as C_n and C_{n+1} (or B_{n+1}), respectively, and A_nA_{n+1} is defined as the RSL corresponding to the stress path C_nC_{n+1} in this study.

With respect to unloading conditions, the deformation of

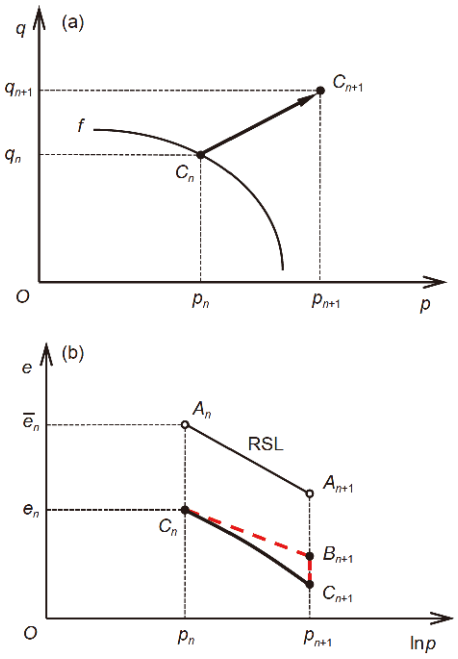

Figure 1 (Color online) Illustration of instant and delayed deformation processes under loading conditions. (a) The stress path under general stress state; (b) the loading-deformation process.

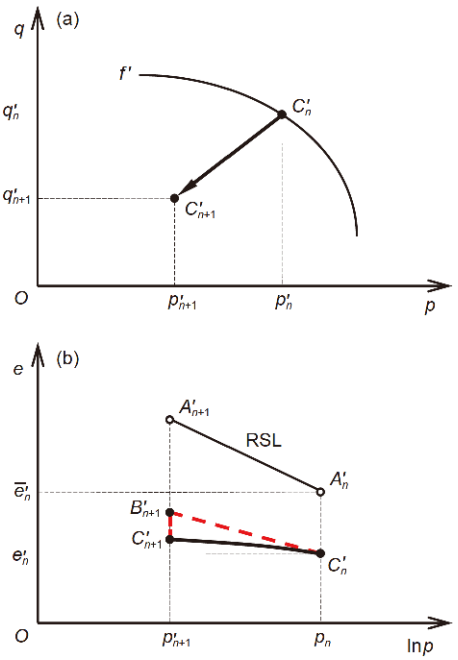

Figure 2 (Color online) Illustration of instant and delayed deformation processes under unloading conditions. (a) The stress path under general stress state; (b) the unloading-deformation process.

clays includes an elastic part and a viscous part. When the clay is unloaded from stress points C'_n to C'_{n+1} with time duration dt as shown in Figure 2(a), in the e-ln$p$ plane, $C'_nC'_{n+1}$ is decomposed into an instant process $C'_nB'_{n+1}$ and a delayed process $B'_{n+1}C'_{n+1}$ as shown in Figure 2(b). The elastic strain increment of $C'_nB'_{n+1}$ can be determined by existing EP models. The viscous strain increment of $B'_{n+1}C'_{n+1}$ is determined by dt and $\mathrm{OCR}_{B'_{n+1}}$, and $\mathrm{OCR}_{B'_{n+1}}$ is obtained by the difference in the void ratio between A'_{n+1} and B'_{n+1}. Here, A'_n and A'_{n+1} denote the normal consolidation state points under the same stress conditions as C'_n and C'_{n+1} (or B'_{n+1}), respectively, and $A'_nA'_{n+1}$ is the RSL corresponding to the stress path $C'_nC'_{n+1}$.

Based on the decomposition of instant and delayed strain increments in the e-ln$p$ plane for clays, a new method is proposed to develop existing EP models into EPV models. In the proposed method, the influences of current stress state and OCR on plastic strain increment and viscous strain increment are separately considered. The existing EP model for normally consolidated clays is improved and subsequently used to calculate the elastic-plastic strain increment for overconsolidated clays. The concept of RSL under general stress state is proposed to determine OCR at the beginning of the delayed deformation process. The viscous flow rule associated with OCR is applied to calculate the viscous strain increment for overconsolidated clays.

2.1 Elastic-plastic strain increments

The elastic-plastic strain increments of C_nB_{n+1} in Figure 1 should be determined by constitutive models for overconsolidated clays. Therefore, if the existing EP model is an overconsolidated clay model, it can be directly used to determine the elastic-plastic strain increment of C_nB_{n+1}. If the existing EP model only suits for normally consolidated clays, the model can be simply improved by the following method to calculate the elastic-plastic strain increments of C_nB_{n+1}.

2.1.1 Elastic strain increment

The elastic strain increment of C_nB_{n+1} is determined by the existing EP model:

$$\mathrm{d}\varepsilon_{ij}^{\mathrm{e}} = C_{ijkl}\mathrm{d}\sigma_{kl}, \tag{4}$$

where C_{ijkl} is a fourth-order elastic compliance tensor, and σ_{kl} is the stress tensor.

2.1.2 Plastic strain increment

The plastic strain increment of C_nB_{n+1} is determined by plastic modulus that is influenced by current stress state and OCR_{C_n}. In the bounding surface model [34,35], the plastic modulus for overconsolidated soils is related to that for normally consolidated soils via a function of current stress state and OCR. In the UH model [36], an additional coefficient Ω that is a function of current stress state and OCR, is introduced into the plastic multiplier of the MCC model. By referring to the above models, the plastic strain increment of

C_nB_{n+1} is given as follows:

$$\mathrm{d}\varepsilon_{ij}^{\mathrm{p}} = \xi \cdot \mathrm{d}\bar{\varepsilon}_{ij}^{\mathrm{p}}, \tag{5}$$

where $\mathrm{d}\bar{\varepsilon}_{ij}^{\mathrm{p}}$ is the plastic strain increment determined by the existing EP model for normally consolidated clays. ξ reflects the influence of current stress state and OCR on the plastic strain increment, which can be written as

$$\xi = \xi\left(\sigma_{ij}, \mathrm{OCR}\right), \tag{6}$$

where OCR is calculated by

$$\mathrm{OCR} = \exp[(\bar{e} - e)/(\lambda - \kappa)], \tag{7}$$

where λ and κ are slopes of the instant isotropic compression line and swelling line, respectively, in the e-ln$p$ plane. $\bar{e}$ is the void ratio that is obtained if the sample is normally consolidated at the current stress state, the determination of $\bar{e}$ is dependent on loading-unloading conditions, which are given by eqs. (10) and (11), respectively. The detailed analysis of eq. (7) is presented in section 3.2.

Combining eqs. (4) and (5), the total elastic-plastic strain increments are expressed as

$$\mathrm{d}\varepsilon_{ij}^{\mathrm{s}} = C_{ijkl}\mathrm{d}\sigma_{kl} + \xi \cdot \mathrm{d}\bar{\varepsilon}_{ij}^{\mathrm{p}}. \tag{8}$$

2.1.3 *Loading-unloading criterion*

The loading-unloading criterion is a function to determine whether the plastic strain increment occurs. It is determined by the angle α between the stress increment vector $\mathrm{d}\sigma_{ij}$ and the external normal to yield surface $\partial f / \partial \sigma_{ij}$. Loading occurs when $\alpha<\pi/2$. Neutral loading occurs when $\alpha=\pi/2$. Unloading occurs when $\alpha>\pi/2$. The loading-unloading criterion is expressed by the following equation:

$$\begin{cases} \dfrac{\partial f}{\partial \sigma_{ij}},\ \mathrm{d}\sigma_{ij} > 0,\ \text{loading}, \\ \dfrac{\partial f}{\partial \sigma_{ij}},\ \mathrm{d}\sigma_{ij} = 0,\ \text{neutral loading}, \\ \dfrac{\partial f}{\partial \sigma_{ij}},\ \mathrm{d}\sigma_{ij} < 0,\ \text{unloading}, \end{cases} \tag{9}$$

where f is the yield function of the existing EP model, and f passes the current stress point C_n. The geometric meaning of the loading-unloading criterion is shown in Figure 3.

It is important to note that the loading-unloading criterion is much simpler than that of the NSFS models, since it only depends on stress increment and is not influenced by time. In this case, the size of f is not affected by time, either. The plastic and viscous strains are separated, and both of them are easy to determine. The viscous strain keeps constant during the instant deformation process regardless of loading or unloading.

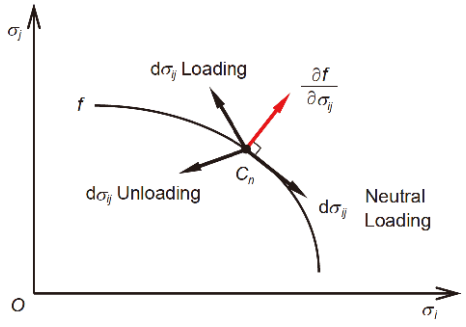

Figure 3 (Color online) Loading-unloading conditions.

2.2 Viscous strain increment

2.2.1 *Reference state line*

The RSL provides a reference to determine $\mathrm{OCR}_{B_{n+1}}$ and $\mathrm{OCR}_{B'_{n+1}}$ that are used to calculate viscous strain increment of $B_{n+1}C_{n+1}$ in Figure 1 and $B'_{n+1}C'_{n+1}$ in Figure 2, respectively.

With respect to the loading condition shown in Figure 1, the RSL is the instant loading line that passes point A_n under the stress path C_nC_{n+1}. The void ratio $\bar{e}_{n+1}$ of point A_{n+1} is calculated by the RSL:

$$\bar{e}_{n+1} = \bar{e}_n - \left(\mathrm{d}\bar{\varepsilon}_{\mathrm{v}}^{\mathrm{e}} + \mathrm{d}\bar{\varepsilon}_{\mathrm{v}}^{\mathrm{p}}\right) \cdot (1 + \bar{e}_0), \tag{10}$$

where $\bar{e}_n$ is the void ratio of point A_n, $\mathrm{d}\bar{\varepsilon}_{\mathrm{v}}^{\mathrm{e}}$ and $\mathrm{d}\bar{\varepsilon}_{\mathrm{v}}^{\mathrm{p}}$ are the elastic and plastic volumetric strain increment, respectively, under the stress path C_nC_{n+1}, and $\bar{e}_0$ is the initial void ratio for normally consolidated clay under consolidation pressure p_0.

With respect to the unloading condition shown in Figure 2, the RSL is a straight line that passes point A'_n. The slope of the RSL denotes the ratio of $\mathrm{d}\bar{e}\big|_{C'_{n+1}C'_n}$ to $\ln\left(p'_{n+1}/p'_n\right)$. Noted that the slope in this study denotes the absolute value of the slope. Specifically, $\mathrm{d}\bar{e}\big|_{C'_{n+1}C'_n}$ is the void ratio increment when the clay is instantaneously loaded from stress point C'_{n+1} to C'_n. Additionally, $\bar{e}'_{n+1}$ of point A'_{n+1} can be determined by the RSL and the void ratio $\bar{e}'_n$ of point A'_n

$$\bar{e}'_{n+1} = \bar{e}'_n - \left(\mathrm{d}\bar{\varepsilon}_{\mathrm{v}}^{\mathrm{e}} - \mathrm{d}\bar{\varepsilon}_{\mathrm{v}}^{\mathrm{p}}\big|_{C'_{n+1}C'_n}\right) \cdot (1 + \bar{e}_0), \tag{11}$$

where $\mathrm{d}\bar{\varepsilon}_{\mathrm{v}}^{\mathrm{p}}\big|_{C'_{n+1}C'_n}$ is the plastic volumetric strain increment under the stress path $C'_{n+1}C'_n$.

Thus, under isotropic compression conditions, the RSL degenerates into the instant isotropic compression line (IICL) for clays under the normal consolidation state. In this case, the RSL is a special RTL that corresponds to the infinity loading strain rate. As shown in Figure 4, the RSL is described as

$$\bar{e}_{n+1} = \bar{e}_n - \lambda \ln \frac{p_{n+1}}{p_n}. \tag{12}$$

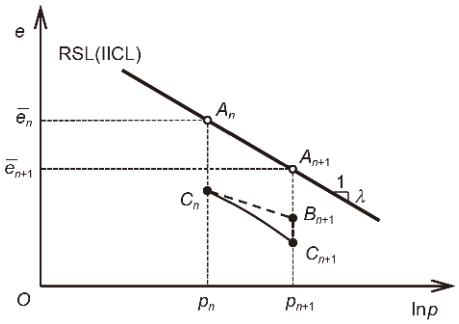

Figure 4 The reference state line under isotropic compression conditions.

2.2.2 *Viscous strain increment under isotropic compression conditions*

The viscous deformation law for clays under isotropic compression conditions is typically described by a logarithmic function. In this paper, the creep behaviour is denoted by

$$e_{B_{n+1}} = \bar{e}_{n+1} - \psi \ln(\bar{t} + 1), \tag{13}$$

where $e_{B_{n+1}}$ is the void ratio in a creep process, as shown by B_{n+1} in Figure 5(a); $\bar{t}$ is the time required to creep from point A_{n+1} on the RSL to point B_{n+1}; ψ is the slope of the secondary consolidation line in the e-ln($\bar{t}$+1) plane as shown in Figure 5(b).

Differentiating eq. (13), the void ratio increment of B_{n+1} at time duration $\mathrm{d}\bar{t}$ is obtained:

$$\mathrm{d}e = -\frac{\psi}{\bar{t}+1}\mathrm{d}\bar{t}. \tag{14}$$

In a creep process, the increment of $\bar{t}$ is equal to that of real time t, and substituting $\mathrm{d}\bar{t} = \mathrm{d}t$ into eq. (14) yields

$$\mathrm{d}e = -\frac{\psi}{\bar{t}+1}\mathrm{d}t. \tag{15}$$

Eq. (13) yields the difference in the void ratio between points A_{n+1} and B_{n+1}.

$$\Delta e_{B_{n+1}} = \bar{e}_{n+1} - e_{B_{n+1}} = \psi \ln(\bar{t} + 1). \tag{16}$$

Substituting eq. (16) into eq. (7), $\bar{t}$ is expressed as follows:

$$\bar{t} = \mathrm{OCR}_{B_{n+1}}^{\theta} - 1, \tag{17}$$

where θ=(λ–κ)/ψ.

The void ratio increment is evaluated as follows:

$$\mathrm{d}e = -\mathrm{d}\varepsilon_{\mathrm{v}} \cdot (1 + e_0), \tag{18}$$

where e_0 is the initial void ratio under consolidation pressure p_0; $\mathrm{d}\varepsilon_{\mathrm{v}}$ is the total volumetric strain increment. In a creep process, only viscous deformation occurs, i.e., $\mathrm{d}\varepsilon_{\mathrm{v}} = \mathrm{d}\varepsilon_{\mathrm{v}}^{\mathrm{v}}$. In this case, eq. (18) is denoted by

$$\mathrm{d}e = -\mathrm{d}\varepsilon_{\mathrm{v}}^{\mathrm{v}} \cdot (1 + e_0). \tag{19}$$

Substituting eqs. (17) and (19) into eq. (15) gives the viscous volumetric strain increment of point B_{n+1} under isotropic compression conditions

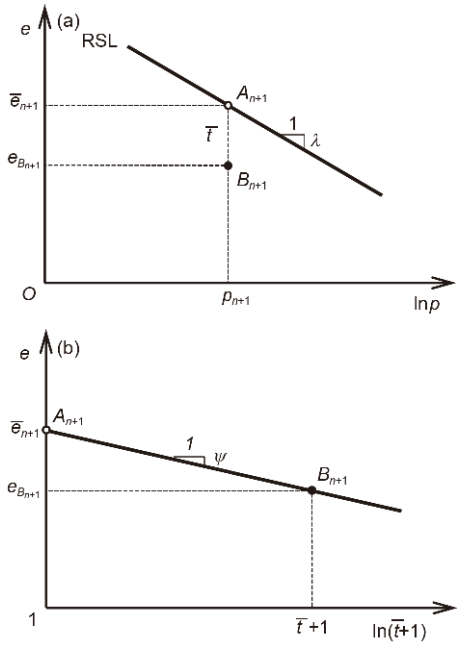

Figure 5 Viscous deformation law under isotropic compression conditions. (a) Changes of void ratio in the e-ln$p$ plane; (b) changes of void ratio in the e-ln$t$ plane.

$$\mathrm{d}\varepsilon_{\mathrm{v}}^{\mathrm{v}} = \frac{\psi}{1+e_0}\frac{\mathrm{d}t}{\mathrm{OCR}_{B_{n+1}}^{\theta}}. \tag{20}$$

2.2.3 *Viscous strain increment under general stress conditions*

In time-dependent models, the viscous strain rate under general stress conditions is typically determined based on the viscous flow rule

$$\dot{\varepsilon}_{ij}^{\mathrm{v}} = \Lambda^{\mathrm{v}}\frac{\partial g^{\mathrm{v}}}{\partial \sigma_{ij}}, \tag{21}$$

where g^{v} is a viscous potential function, and Λ^{v} is a viscous multiplier. There are mainly two approaches to determine Λ^{v} [37]: (1) the viscous potential surface denoted by g^{v} is considered as an isosurface of the viscous volumetric strain rate $\dot{\varepsilon}_{\mathrm{v}}^{\mathrm{v}}$ [31,38,39], nevertheless, models adopting the method fails to predict the critical state of clays [40]; (2) the viscous potential surface is considered as an isosurface of Λ^{v} [26,27,41], and models established by the method reasonably reproduce critical state conditions [26]. Therefore, the second approach is adopted to determine Λ^{v} in this study.

The viscous volumetric strain rate is obtained from eq. (21):

$$\dot{\varepsilon}_{\mathrm{v}}^{\mathrm{v}} = \Lambda^{\mathrm{v}}\frac{\partial g^{\mathrm{v}}}{\partial p}. \tag{22}$$

Under isotropic compression conditions, eq. (22) is written as

$$\left(\dot{\varepsilon}_{\mathrm{v}}^{\mathrm{v}}\right)_{\mathrm{iso}} = \Lambda^{\mathrm{v}}\left(\frac{\partial g^{\mathrm{v}}}{\partial p}\right)_{\mathrm{iso}}, \tag{23}$$

where the subscript "iso" denotes isotropic compression conditions.

The viscous volumetric strain rates under isotropic stress conditions is obtained from eq. (20).

$$\left(\dot{\varepsilon}_{\mathrm{v}}^{\mathrm{v}}\right)_{\mathrm{iso}}=\frac{\psi}{(1+e_0)}\frac{1}{\mathrm{OCR}_{B_{n+1}}^{\theta}}. \tag{24}$$

Substituting eq. (24) into eq. (23), Λ^{v} is determined:

$$\Lambda^{\mathrm{v}}=\frac{\psi}{(1+e_0)\mathrm{OCR}_{B_{n+1}}^{\theta}}\frac{1}{(\partial g^{\mathrm{v}}/\partial p)_{\mathrm{iso}}}. \tag{25}$$

Thus, the viscous strain increment of $B_{n+1}C_{n+1}$ in Figure 1 is calculated by

$$\mathrm{d}\varepsilon_{ij}^{\mathrm{v}}=\dot{\varepsilon}_{ij}^{\mathrm{v}}\cdot\mathrm{d}t=\Lambda^{\mathrm{v}}\frac{\partial g^{\mathrm{v}}}{\partial\sigma_{ij}}\mathrm{d}t. \tag{26}$$

Substituting eq. (25) into eq. (26) gives the viscous strain increment of $B_{n+1}C_{n+1}$.

$$\mathrm{d}\varepsilon_{ij}^{\mathrm{v}}=\frac{\psi}{(1+e_0)\mathrm{OCR}_{B_{n+1}}^{\theta}}\frac{1}{(\partial g^{\mathrm{v}}/\partial p)_{\mathrm{iso}}}\frac{\partial g^{\mathrm{v}}}{\partial\sigma_{ij}}\mathrm{d}t. \tag{27}$$

2.3 Time-dependent deformation behaviours of clays

The time-dependent deformation behaviours of clays mainly include creep, stress relaxation and strain rate effects. The aforementioned behaviours are discussed in detail under isotropic compression conditions in the following sections.

2.3.1 Creep

Creep is the process of deformation with time when the clay is subjected to a constant external load. With respect to any point C_n under isotropic compression conditions, the creep process C_nC_{n+1} within time duration dt is shown in Figure 6 (a). The creep rate $\dot{\varepsilon}_{\mathrm{cr}}$ (i.e., viscous volumetric strain rate) is obtained by substituting eq. (7) into eq. (24)

$$\dot{\varepsilon}_{\mathrm{cr}}=\frac{\psi}{1+e_0}\frac{1}{\exp[\Delta e\cdot\theta/(\lambda-\kappa)]}. \tag{28}$$

Eq. (28) indicates that $\dot{\varepsilon}_{\mathrm{cr}}$ is a monotonically decreasing function of Δe. Given that $\Delta e_{C_n}<\Delta e_{C_{n+1}}$, the $\dot{\varepsilon}_{\mathrm{cr}}$ at point C_n ($\dot{\varepsilon}_{\mathrm{cr}|C_n}$) exceeds $\dot{\varepsilon}_{\mathrm{cr}|C_{n+1}}$. The void ratio of clay decreases when the creep process continues, hereby resulting in increased density. Thus, as shown in Figure 6(b), the creep rate slows down with the increase of Δe.

2.3.2 Stress relaxation

Stress relaxation refers to the phenomenon that the stress in clays decreases with time under constant strain. Although the stress relaxation tests are not extensively studied compared to creep tests, they may also provide a way to determine viscous parameters of soft soils [42]. With respect to any point C_{n-1} under isotropic compression conditions, two successive stress relaxation steps $C_{n-1}C_n$ and C_nC_{n+1} with the same time duration dt are shown in Figure 7(a). Each step is divided into instant rebounding with a constant slope of κ in the e-ln$p$ plane and creep. The feature of stress relaxation under isotropic compression conditions is that the instant rebounding volumetric deformation is equal to that of the creep, and thus the void ratios of C_{n-1}, C_n and C_{n+1} are identical.

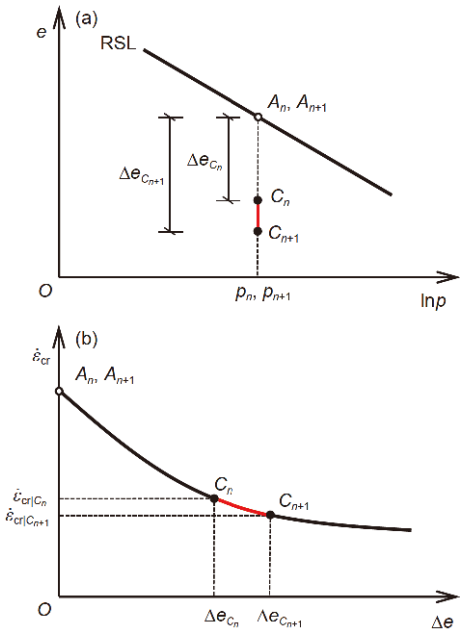

Figure 6 (Color online) Response of clay in a creep process. (a) The stress path; (b) changes of the creep rate versus the void ratio difference.

Given that $\Delta e_{B_{n+1}}>\Delta e_{B_n}$, the creep rate $\dot{\varepsilon}_{\mathrm{cr}|B_{n+1}}<\dot{\varepsilon}_{\mathrm{cr}|B_n}$ as indicated by eq. (28). Thus, the void ratio difference between B_{n+1} and C_{n+1} (=V$\dot{\varepsilon}_{\mathrm{cr}|B_{n+1}}\mathrm{d}t$, where V=1+$e_0$) is less than that between B_n and C_n (=V$\dot{\varepsilon}_{\mathrm{cr}|B_n}\mathrm{d}t$). The slopes of C_nB_{n+1} and $C_{n-1}B_n$ are all equal to κ, and thus $\ln(p_n/p_{n+1})<\ln(p_{n-1}/p_n)$. As the time durations corresponding to p_np_{n+1} and $p_{n-1}p_n$ are identical, the mean stress rate $\dot{p}/p$ decreases with time as shown in Figure 7(b).

2.3.3 Strain rate effects

Strain rate effects refer to the phenomenon that the stress-strain behaviours of clays are affected by the strain rates. This phenomenon can be explained as that the deformation proportions caused by load and time are different at various strain rates. In this section, the strain rate effects are analysed in detail under the condition of constant strain rates.

Yao et al. [15] proposed the concept of characteristic strain rate. When the clay in state point C_n is loaded at a specific strain rate and the slope of isotropic compression line is λ as shown in Figure 8, then the rate is called characteristic strain rate. The characteristic strain rate reflects the correspondence between loading rate and OCR. It is obtained by the following derivation.

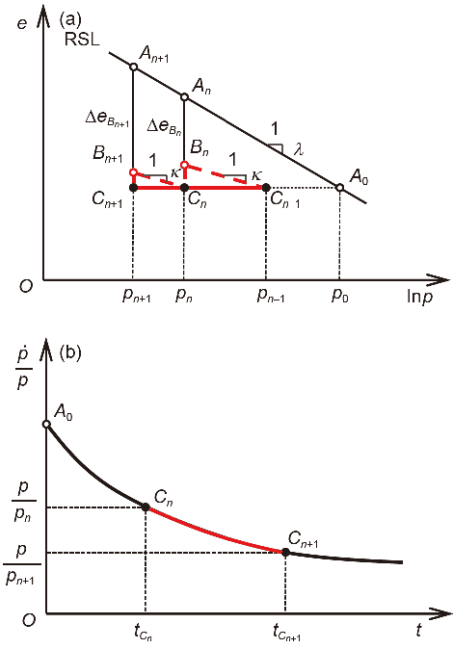

Figure 7 (Color online) Response of clay in a stress relaxation process. (a) The stress path; (b) changes of the stress rate with time.

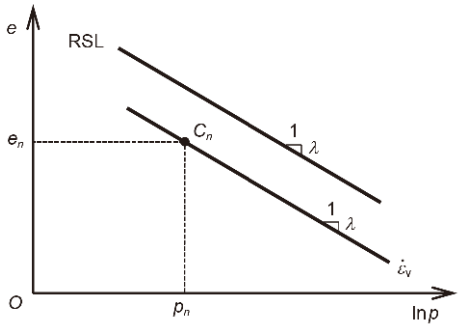

Figure 8 The characteristic strain rate.

The instant volumetric strain increment for overconsolidated soil is given as (for details about the derivation of eq. (29), refer to Appendix)

$$\mathrm{d}\varepsilon_{\mathrm{v}}^{\mathrm{s}} = \frac{\kappa}{1+e_0}\frac{\mathrm{d}p}{p} + \xi_{\mathrm{iso}}\frac{\lambda-\kappa}{1+\bar{e}_0}\frac{\mathrm{d}p}{p}, \tag{29}$$

where ξ_{iso} denotes the value of ξ under isotropic compression conditions. With respect to overconsolidated clays, the slope of the instant isotropic loading line increases, and OCR decreases with increases in p in the e-ln$p$ plane [43,44] as shown in Figure 9. The plastic modulus decreases with decreases in OCR. Therefore, ξ_{iso} is a monotonically decreasing function of OCR, which can be expressed as

$$\xi_{\mathrm{iso}} = \xi_{\mathrm{iso}}(\mathrm{OCR}). \tag{30}$$

Substituting eqs. (20) and (30) into eq. (3), the total strain increment under isotropic stress conditions is

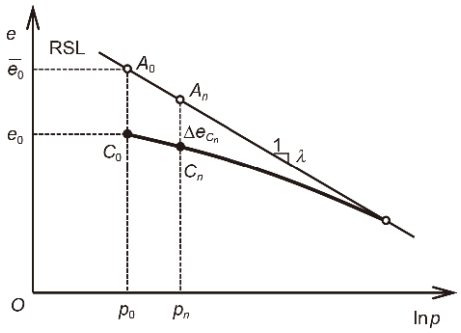

Figure 9 The instant compression line for overconsolidated clays under isotropic compression conditions.

$$\mathrm{d}\varepsilon_{\mathrm{v}} = \frac{\kappa}{1+e_0}\frac{\mathrm{d}p}{p} + \xi_{\mathrm{iso}}\frac{\lambda-\kappa}{1+\bar{e}_0}\frac{\mathrm{d}p}{p} + \frac{\psi}{1+e_0}\mathrm{OCR}^{-\theta}\mathrm{d}t. \tag{31}$$

At the characteristic strain rate, dp/p in eq. (31) can be expressed as

$$\frac{\mathrm{d}p}{p} = -\frac{\mathrm{d}e}{\lambda}. \tag{32}$$

Substituting eq. (32) into eq. (31) yields

$$\mathrm{d}\varepsilon_{\mathrm{v}} = \frac{\kappa}{1+e_0}\frac{-\mathrm{d}e}{\lambda} + \xi_{\mathrm{iso}}\frac{\lambda-\kappa}{1+\bar{e}_0}\frac{-\mathrm{d}e}{\lambda} + \frac{\psi}{1+e_0}\mathrm{OCR}^{-\theta}\mathrm{d}t. \tag{33}$$

Substituting eq. (18) into eq. (33), the characteristic strain rate is obtained.

$$\dot{\varepsilon}_{\mathrm{ch}} = \frac{\lambda}{\lambda-\kappa}\frac{\psi}{1+e_0}\mathrm{OCR}^{-\theta}\cdot\left(1-\xi_{\mathrm{iso}}\frac{1+e_0}{1+\bar{e}_0}\right)^{-1}. \tag{34}$$

Eq. (34) indicates that $\dot{\varepsilon}_{\mathrm{ch}}$ is a monotonically decreasing function of OCR. The OCRs of state points that are on a line parallel to the RSL are the same, thereby indicating that $\dot{\varepsilon}_{\mathrm{ch}}$ of the aforementioned state points is a constant value. Therefore, the compression line is parallel to RSL when the overconsolidated clays are loaded at a constant strain rate of $\dot{\varepsilon}_{\mathrm{ch}}$.

Under isotropic compression conditions, the initial state point is indicated by C_0 as shown in Figure 10. The value of the strain rate significantly affects the initial slope of the loading curve. There are four special cases for the initial slope that are associated with four strain rates: (1) when the strain rate is infinity, all deformation corresponds to instant deformation caused only by the load, and no viscous deformation associated with time is produced. The initial slope of the loading curve is $\kappa+\xi_{\mathrm{iso}}(\lambda-\kappa)(1+e_0)/(1+\bar{e}_0)$ as indicated by eq. (29); (2) when the loading strain rate equals to the characteristic rate of C_0, $\dot{\varepsilon}_{\mathrm{ch}}|_{C_0}$, the initial slope of the loading curve is λ; (3) when the loading strain rate equals to $\dot{\varepsilon}_{\mathrm{ch}}|_{C_0}$, all the deformation corresponds to viscous deformation. The initial slope of the loading curves is infinity; (4) when the loading strain rate is zero, it is a stress relaxation phenomenon. The initial slope of the loading curve is zero. In this case, the deformation of the clay is elastic-viscous. The

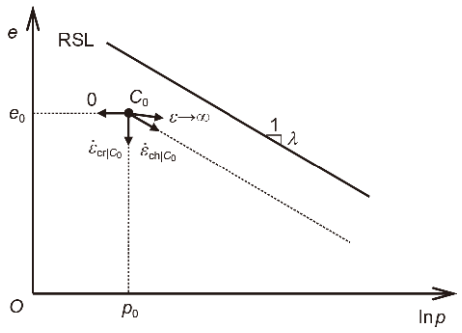

Figure 10 Initial slopes of the isotropic compression curves at constant strain rates.

elastic recovery deformation balances with the viscous deformation, the total deformation is zero, and mean stress p decreases.

The above four loading strain rates divide the possible loading curves into three conditions.

With respect to the condition that the constant loading strain rate $\dot{\varepsilon}$ exceeds $\dot{\varepsilon}_{ch|C_0}$, the initial slope of the loading curve is less than λ as shown in Figure 11(a). In any loading process C_nC_{n+1}, OCR of the clay decreases as shown in Figure 11(b), and $\dot{\varepsilon}_{ch}$ of current point increases based on eq. (34). When $\dot{\varepsilon}_{ch}$ reaches $\dot{\varepsilon}$, the loading curve becomes a straight line with a slope of λ.

With respect to the condition that $\dot{\varepsilon}_{cr|C_0} < \dot{\varepsilon} < \dot{\varepsilon}_{ch|C_0}$, the initial slope of the loading curve exceeds λ as shown in Figure 12(a). In any loading process C_nC_{n+1}, OCR of the clay increases as shown in Figure 12(b), and $\dot{\varepsilon}_{ch}$ of current point decreases. When $\dot{\varepsilon}_{ch}$ decreases to $\dot{\varepsilon}$, the loading curve slope becomes λ.

With respect to the condition that $\dot{\varepsilon} < \dot{\varepsilon}_{cr|C_0}$, the behaviour of clays is considered as the combination of creep and stress relaxation. In the loading process, p and e decrease as denoted by C_nC_{n+1} in Figure 13(a). Correspondingly, OCR of the clay increases as shown in Figure 13(b), and thus the creep rate decreases as indicated by eq. (24). When the creep rate equals to $\dot{\varepsilon}$, the loading curve slope is infinity as denoted by point C' in Figure 13(a). When the loading process continues, OCR increases and the creep rate decreases. Therefore, $\dot{\varepsilon}$ is between the current creep rate and characteristic strain rate, and the stress-strain behaviours of clay after point C' are similar to that shown in Figure 12.

3 Extended modified cam clay model

The MCC model is a classical EP model for clays. Based on it, several models [45–48] have been developed. In this paper, the MCC model is developed into the extended modified cam clay (EMCC) model by the proposed method. Firstly,

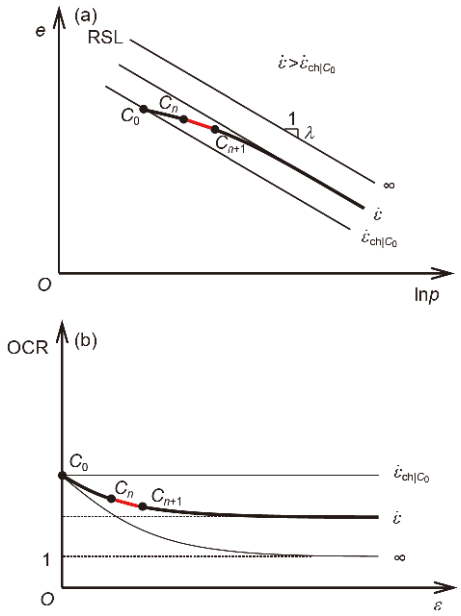

Figure 11 (Color online) Stress-strain behaviours of clays at strain rate higher than initial characteristic rate. (a) The isotropic loading curve; (b) OCR in the loading process.

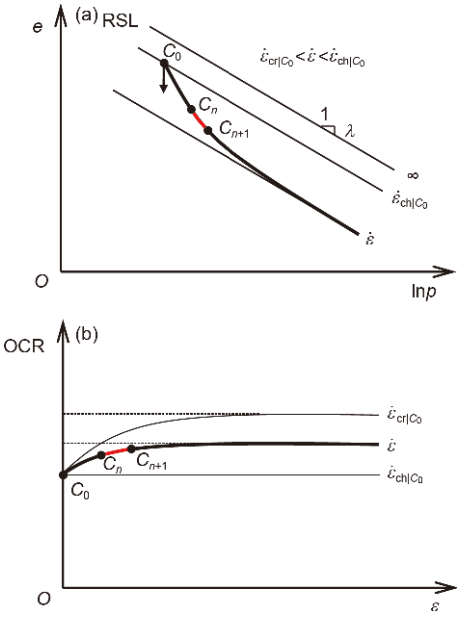

Figure 12 (Color online) Stress-strain behaviours of clays at strain rate higher than initial creep rate and less than initial characteristic rate. (a) The isotropic loading curve; (b) OCR in the loading process.

the RSL is determined based on the MCC model. Then, OCR is obtained by the RSL. On this basis, the stress-strain-time relationship for clays is given.

3.1 Determination of the RSL

With respect to loading conditions, the RSL is the instant loading line that passes point A_n under the stress path C_nC_{n+1}

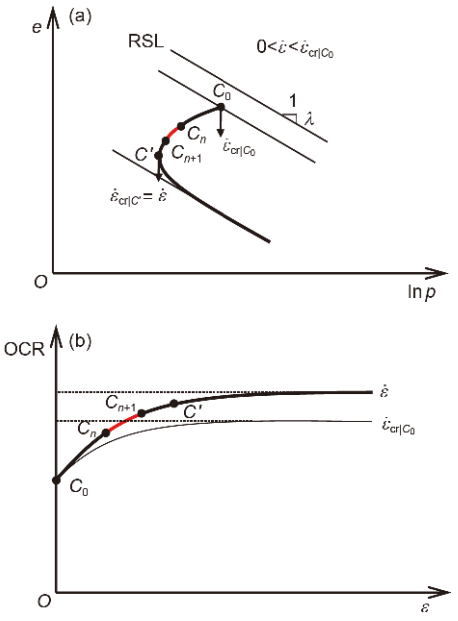

Figure 13 (Color online) Stress-strain behaviours of clays at strain rate less than initial creep rate. (a) The isotropic loading curve; (b) OCR in the loading process.

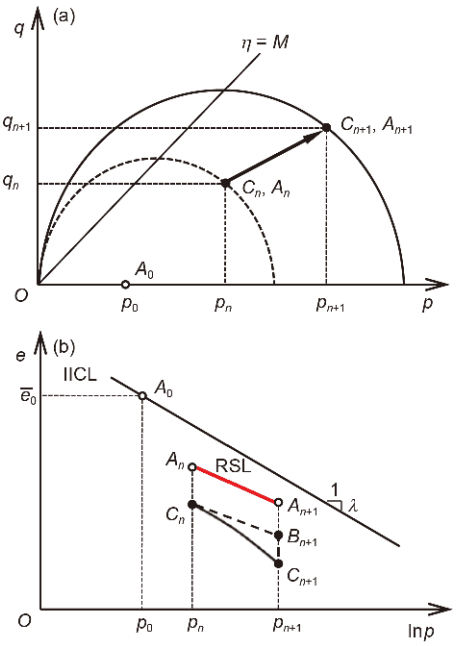

Figure 14 (Color online) Determination of the RSL in the loading condition. (a) The actual stress path in the *p*-*q* plane; (b) the RSL in the *e*-ln*p* plane.

as shown in Figure 14. The stress-strain relationship corresponding to RSL is consistent with that of the MCC model.

$$\mathrm{d}\bar{\varepsilon}_{\mathrm{v}}^{\mathrm{e}}=\frac{\kappa}{(1+\bar{e}_0)p}\mathrm{d}p, \tag{35}$$

$$\mathrm{d}\bar{\varepsilon}_{\mathrm{v}}^{\mathrm{p}}=\frac{\lambda-\kappa}{(1+\bar{e}_0)p}\frac{2\eta}{M^2+\eta^2}\left(\frac{M^2-\eta^2}{2\eta}\mathrm{d}p+\mathrm{d}q\right). \tag{36}$$

When the RSL is determined, the instant volumetric strain increment from A_n to A_{n+1} is obtained by substituting eqs. (35) and (36) into eq. (2). Subsequently, the void ratio $\bar{e}_{n+1}$ of point A_{n+1} is derived from eq. (10) as follows:

$$\bar{e}_{n+1}=\bar{e}_n-\frac{\kappa}{p}\mathrm{d}p+\frac{\lambda-\kappa}{p}\frac{2\eta}{M^2+\eta^2}\left(\frac{M^2-\eta^2}{2\eta}\mathrm{d}p+\mathrm{d}q\right), \tag{37}$$

where η is the stress ratio, and $\eta=q/p$. It should be noted that $\bar{e}_n$ of point A_n in eq. (37) is also calculated identical to A_nA_{n+1} step by step from initial normal consolidation state point A_0.

With respect to unloading conditions, as shown by $C'_nC'_{n+1}$ in Figure 2(a), the value of $-\mathrm{d}\bar{\varepsilon}_{\mathrm{v}}^{\mathrm{p}}\big|_{C'_{n+1}C'_n}$ in eq. (11) is identical to that of $\mathrm{d}\bar{\varepsilon}_{\mathrm{v}}^{\mathrm{p}}$ in eqs. (10) and (36). Therefore, for the EMCC model, the determination method of RSL in unloading conditions is the same to that in loading conditions.

3.2 Determination of OCR

In order to describe the instant process C_nB_{n+1} and the delayed processes $B_{n+1}C_{n+1}$, OCR_{C_n} and $\mathrm{OCR}_{B_{n+1}}$ is required. They are used to calculate plastic and viscous strain increments, respectively. The OCR is determined under both isotropic and triaxial compression conditions.

With respect to isotropic compression conditions, the RSL is the IICL. The preconsolidation pressure p_{cn} is the abscissa of the intersection of the RSL and the swelling line that passes point C_n as shown in Figure 15. The OCR of point C_n is determined by the following equation:

$$\mathrm{OCR}_{C_n}=\frac{p_{cn}}{p_n}=\exp\left[\Delta e_{C_n}/(\lambda-\kappa)\right]. \tag{38}$$

With respect to triaxial compression conditions, the viscous strain increment from point A_n to point C_n is identical to the plastic strain increment from point A_{xn} to point A'_{xn} as shown in Figure 16(a), where points A_{xn} and A'_{xn} are the intersections of the IICL and the swelling lines that pass A_n and C_n, respectively, and A_{xn} and A'_{xn} actually reflect the size of the yield curves as shown in Figure 16(b). The distance between A_{xn} and A'_{xn} is used to calculate OCR_{C_n}.

$$\mathrm{OCR}_{C_n}=\frac{p'_{xn}}{p_{xn}}=\exp\left[\Delta e_{C_n}/(\lambda-\kappa)\right], \tag{39}$$

where p_x is the intersection of the yield surface with the p axis.

This method is similar to that used in the bounding surface model [35] and the UH model [15,36].

Combining eqs. (38) and (39), the OCR_{C_n} under general stress state is uniformly described as

$$\mathrm{OCR}_{C_n}=\exp\left[(\bar{e}_n-e_n)/(\lambda-\kappa)\right]. \tag{40}$$

The determination of $\mathrm{OCR}_{B_{n+1}}$ is indentical to that of

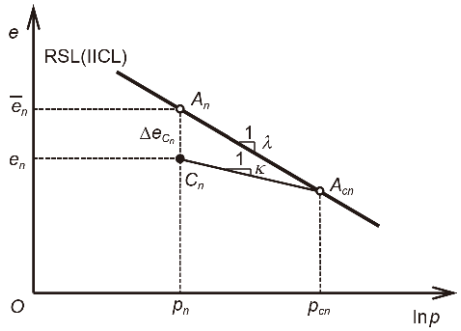

Figure 15 Calculation of OCR under isotropic stress state.

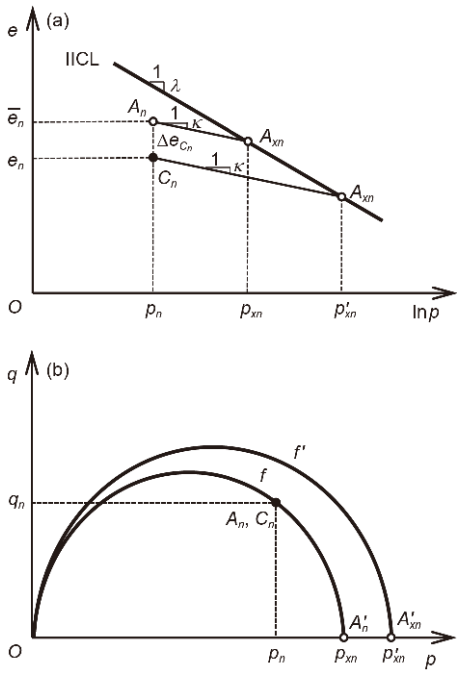

Figure 16 Calculation of OCR under triaxial stress state. (a) The state points in the e-ln$p$ plane; (b) the yield curves in the p-q plane.

OCR_{C_n}, which is written as

$$\mathrm{OCR}_{B_{n+1}} = \exp\left[\left(\bar{e}_{n+1} - e_{B_{n+1}}\right)/(\lambda-\kappa)\right], \tag{41}$$

where $\bar{e}_{n+1}$ is given in eq. (37), and $e_{B_{n+1}}$ is calculated by

$$e_{B_{n+1}} = e_n - \left(\mathrm{d}\varepsilon_{\mathrm{v}}^{\mathrm{e}} + \mathrm{d}\varepsilon_{\mathrm{v}}^{\mathrm{p}}\right)\cdot(1+e_0). \tag{42}$$

3.3 Stress-strain-time relationship of the EMCC model

The main issue in developing the MCC model to the EMCC model specifically lies on the determination of the elastic, plastic and viscous strain increments. In this section, the elastic-plastic strain increments are obtained by improvement of the MCC model, while the viscous strain increment is derived based on the viscous flow rule associated with OCR.

3.3.1 *Elastic strain increment*

The elastic strain increment is the same with the MCC model, and is given by Hooke's law.

$$\begin{aligned}\mathrm{d}\varepsilon_{\mathrm{v}}^{\mathrm{e}} &= \frac{\mathrm{d}p}{K},\\ \mathrm{d}\varepsilon_{\mathrm{d}}^{\mathrm{e}} &= \frac{\mathrm{d}q}{3G},\end{aligned} \tag{43}$$

where K and G are the bulk modulus and shear modulus, respectively.

$$\begin{aligned}K &= \frac{(1+e_0)}{\kappa}p,\\ G &= \frac{3(1-2\nu)}{2(1+\nu)}K,\end{aligned} \tag{44}$$

where ν is the Poisson's ratio.

3.3.2 *Plastic strain increment*

With respect to isotropic compression conditions, the slope of instant compression line in the e-ln$p$ plane decreases with increases in OCR as discussed in section 2.2.3. When OCR equals to 1, the slope is λ, and the slope approaches κ when the value of OCR increases. Thus, the slope of the instant compression line for overconsolidated clays can be denoted by an interpolation between λ and κ based on OCR.

$$\frac{-\mathrm{d}e}{\mathrm{d}(\ln p)} = \kappa + (\lambda-\kappa)\mathrm{OCR}^{-\chi}, \tag{45}$$

where χ is a material parameter that controls the slope of instant compression line.

Based on eq. (18), the void ratio increment in eq. (45) during the instant isotropic loading process is expressed as follows:

$$\mathrm{d}e = -\mathrm{d}\varepsilon_{\mathrm{v}}^{\mathrm{s}}\cdot(1+e_0). \tag{46}$$

Substituting eq. (46) into eq. (45) gives the instant volumetric strain increment:

$$\mathrm{d}\varepsilon_{\mathrm{v}}^{\mathrm{s}} = \frac{\kappa}{1+e_0}\frac{\mathrm{d}p}{p} + \frac{\lambda-\kappa}{1+e_0}\frac{\mathrm{d}p}{p}\mathrm{OCR}^{-\chi}. \tag{47}$$

Comparing eq. (47) with eq. (29), ξ_{iso} is obtained.

$$\xi_{\mathrm{iso}} = \frac{1+\bar{e}_0}{1+e_0}\mathrm{OCR}^{-\chi}. \tag{48}$$

In order to ensure that the model is simple, eq. (48) is directly applied to triaxial compression conditions to determine ξ:

$$\xi_{\mathrm{iso}} = \frac{1+\bar{e}_0}{1+e_0}\mathrm{OCR}^{-\chi}, \tag{49}$$

where the OCR in eq. (49) is determined by triaxial compression conditions.

Based on the MCC model, the plastic volumetric strain increment $\mathrm{d}\bar{\varepsilon}_{\mathrm{v}}^{\mathrm{p}}$ and plastic deviatoric strain increment $\mathrm{d}\bar{\varepsilon}_{\mathrm{d}}^{\mathrm{p}}$ are expressed as

$$\begin{cases} \mathrm{d}\bar{\varepsilon}_{\mathrm{v}}^{\mathrm{p}} = \dfrac{\lambda-\kappa}{(1+\bar{e}_0)p}\dfrac{2\eta}{M^2+\eta^2}\left(\dfrac{M^2-\eta^2}{2\eta}\mathrm{d}p+\mathrm{d}q\right), \\ \mathrm{d}\bar{\varepsilon}_{\mathrm{d}}^{\mathrm{p}} = \dfrac{\lambda-\kappa}{(1+\bar{e}_0)p}\dfrac{2\eta}{M^2+\eta^2}\left(\mathrm{d}p+\dfrac{2\eta}{M^2-\eta^2}\mathrm{d}q\right). \end{cases} \tag{50}$$

Substituting eqs. (49) and (50) into eq. (5) yields the plastic strain increment for the EMCC model.

$$\begin{cases} \mathrm{d}\varepsilon_{\mathrm{v}}^{\mathrm{p}} = \dfrac{\lambda-\kappa}{(1+e_0)p}\dfrac{2\eta\mathrm{OCR}^{-\chi}}{M^2+\eta^2}\left(\dfrac{M^2-\eta^2}{2\eta}\mathrm{d}p+\mathrm{d}q\right), \\ \mathrm{d}\varepsilon_{\mathrm{d}}^{\mathrm{p}} = \dfrac{\lambda-\kappa}{(1+e_0)p}\dfrac{2\eta\mathrm{OCR}^{-\chi}}{M^2+\eta^2}\left(\mathrm{d}p+\dfrac{2\eta}{M^2-\eta^2}\mathrm{d}q\right). \end{cases} \tag{51}$$

3.3.3 *Viscous strain increment*

The viscous potential function g^{v} is in the same form as the plastic potential function of the MCC model.

$$g^{\mathrm{v}} = p^2 + \frac{q^2}{M^2} - pp_x. \tag{52}$$

The partial derivatives of eq. (52) with respect to p and q are

$$\begin{cases} \dfrac{\partial g^{\mathrm{v}}}{\partial p} = 2p - p_x, \\ \dfrac{\partial g^{\mathrm{v}}}{\partial q} = \dfrac{2q}{M^2}. \end{cases} \tag{53}$$

Under isotropic compression conditions, by substituting p=p_x into eq. (53), one obtains

$$\left(\frac{\partial g^{\mathrm{v}}}{\partial p}\right)_{\mathrm{iso}} = p_x, \tag{54}$$

where p_x in eq. (54) is obtained based on eq. (52).

$$p_x = \frac{p^2M^2+q^2}{pM^2}. \tag{55}$$

Substituting eqs. (53)–(55) into eq. (27) yields the viscous volumetric strain increment $\mathrm{d}\varepsilon_{\mathrm{v}}^{\mathrm{v}}$ and viscous deviatoric strain increment $\mathrm{d}\varepsilon_{\mathrm{d}}^{\mathrm{v}}$.

$$\begin{cases} \mathrm{d}\varepsilon_{\mathrm{v}}^{\mathrm{v}} = \dfrac{\psi}{1+e_0}\dfrac{1}{\mathrm{OCR}^{\theta}}\dfrac{M^2-\eta^2}{M^2+\eta^2}\mathrm{d}t, \\ \mathrm{d}\varepsilon_{\mathrm{d}}^{\mathrm{v}} = \dfrac{\psi}{1+e_0}\dfrac{1}{\mathrm{OCR}^{\theta}}\dfrac{2\eta}{M^2+\eta^2}\mathrm{d}t. \end{cases} \tag{56}$$

3.4 Determination of parameters

The EMCC model includes six independent material parameters and a model parameter: M, λ, κ, υ, ψ, χ and $\bar{e}_0$. Four of the aforementioned parameters, i.e., M, λ, κ and υ are identical to the material parameters in the MCC model, and the determination methods are identical to those of the MCC model.

Material parameters ψ and χ and the model parameter $\bar{e}_0$ are determined by isotropic compression tests. ψ is the slope of secondary consolidation line. χ is determined by two groups of isotropic compression tests loaded at constant strain rate $\dot{\varepsilon}_1$ and $\dot{\varepsilon}_2$ as shown in Figure 17. The corresponding loading curves reach two parallel lines with a slope of λ. Two points when p=p_{12} on the parallel part of the loading curves are thereby obtained, i.e., $D_1(p_{12}, e_1)$ and D_2 (p_{12}, e_2). The characteristic strain rates at points D_1 and D_2 are $\dot{\varepsilon}_1$ and $\dot{\varepsilon}_2$, respectively. Equations on the characteristic rate are obtained by substituting eq. (48) into eq. (34) as follows:

$$\dot{\varepsilon}_1 = \frac{\lambda}{\lambda-\kappa}\frac{\psi}{1+e_0}\mathrm{OCR}_{D_1}^{-\theta}\cdot\left(1-\mathrm{OCR}_{D_1}^{-\chi}\right)^{-1}, \tag{57}$$

$$\dot{\varepsilon}_2 = \frac{\lambda}{\lambda-\kappa}\frac{\psi}{1+e_0}\mathrm{OCR}_{D_2}^{-\theta}\cdot\left(1-\mathrm{OCR}_{D_2}^{-\chi}\right)^{-1}. \tag{58}$$

Furthermore, OCR_{D_1} and OCR_{D_2} are obtained from eq. (38), and thus, the ratio of OCR_{D_1} to OCR_{D_2} is expressed as

$$\frac{\mathrm{OCR}_{D_1}}{\mathrm{OCR}_{D_2}} = \exp\left[\frac{e_2-e_1}{\lambda-\kappa}\right]. \tag{59}$$

Three unknown quantities (i.e., χ, OCR_{D_1} and OCR_{D_2}) are collectively solved by eqs. (57), (58), and (59). Thus, χ is determined.

The model parameter $\bar{e}_0$ is determined by OCR_{D_1} or OCR_{D_2} and its determination method is identical. Therefore, only take OCR_{D_1} as an example. The difference in the void ratio between A_{12} and D_1 in Figure 17 is Δe_{D_1}=$(\lambda-\kappa)\cdot\ln\mathrm{OCR}_{D_1}$ as indicated by eq. (38). Thus, the state point A_{12} is obtained. The RSL with slope λ that passes point A_{12} is determined, and $\bar{e}_0$ of point A_0 that is also on the RSL is derived as

$$\bar{e}_0 = e_1+(\lambda-\kappa)\cdot\ln\mathrm{OCR}_{D_1}+\lambda\left(\ln p_0-\ln p_{12}\right). \tag{60}$$

Additionally, the parameters can also be identified by optimization methods [49–51] when the tests mentioned above are limited.

3.5 Verification of the EMCC model

The EMCC model is applied to predict drained oedometer

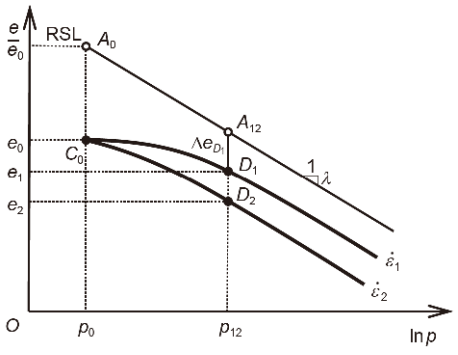

Figure 17 Determination of χ and $\bar{e}_0$.

tests on Wenzhou clay [52], undrained triaxial compression tests on San Francisco Bay Mud (SFBM) [53] and soft Hong Kong marine deposits (HKMD) [6]. Clay parameters are listed in Table 1.

3.5.1 *Drained oedometer tests at step-changed axial strain rate*

Yin et al. [52] conducted drained oedometer tests on Wenzhou clay. The initial consolidation pressure was 10 kPa. The samples were compressed at step-changed axial strain rate. The axial strain rates in Test 1 (Figure 18(a)) are 0.2%/h, 20%/h, 2%/h, 20%/h and 0.2%/h successively, while those in Test 2 (Figure 18(b)) are 2%/h, 20%/h, 0.2%/h, 20%/h and 0.2%/h. The soil parameters are presented in Table 1. M, λ, κ and v are from Yin et al. [52]. ψ and χ are calibrated from the test results shown in Figure 18(a). The initial void ratio is 1.89 and initial OCR is about 10, so $\bar{e}_0$ is determined as 2.677 according to eq. (7).

Figure 18 compares the measured and predicted relationship between void ratio e and vertical stress σ_1. Test results show that the larger the strain rate is, the upper the loading curve will be. The predictions are in excellent consistency with the measured result. The EMCC model captures the stress-strain behavior of Wenzhou clay induced by strain rate.

3.5.2 *Undrained triaxial compression test at step-changed axial strain rate*

Lacerda [53] provided data of undrained triaxial compression test at step-changed axial strain rate test on SFBM. The loading procedures are shown in Figure 19. The axial strain rate $\dot{\varepsilon}_1$ was changed many times combined with stress relaxation processes. The initial consolidation pressure was 78.5 kPa. The clay parameters are listed in Table 1. M, λ, κ and v are from Jiang et al. [54]. $\bar{e}_0$ and χ are calibrated from the data at $\dot{\varepsilon}_1 = 1.52\,\%/\mathrm{min}$. ψ is calibrated from the data during the first stress relaxation process. The initial OCR is adopted as 1.15.

Figure 19(a) presents the variation of deviator stress with axial strain, and Figure 19(b) shows the effective stress path. When the axial strain is constant, the deviator stress gradually decreases. The EMCC model can reasonably reproduce the stress relaxation phenomenon of SFBM, as indicated by the comparisons between measured and predicted results.

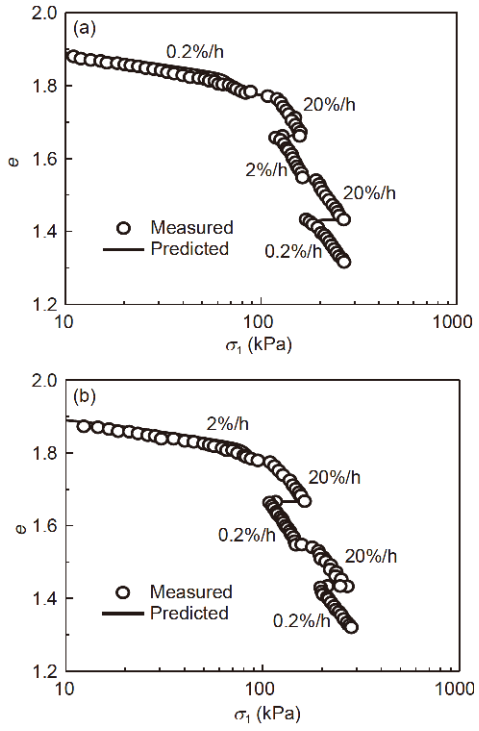

Figure 18 Comparisons between measured and predicted results for drained oedometer tests at step-changed axial strain rate. (a) Test 1; (b) test 2.

3.5.3 *Undrained triaxial compression tests at constant strain rate*

Undrained triaxial compression tests on HKMD at constant strain rate were performed by Zhu [6]. The initial consolidation pressure was 400 kPa. The specimens were sheared at constant deviatoric strain rate of 0.25, 0.025%/min and 0.0025%/min. The clay parameters are listed in Table 1. M, λ, κ, v and ψ are from Zhu [6]. χ is calibrated by test results loaded at constant strain rate of 0.25%/min and 0.0025%/min. The initial void ratio e_0 is 0.949 at p_0= 400 kPa, and the initial OCR is estimated to be 1.1 according to the comparison between model prediction and test results. Thus, $\bar{e}_0$ is determined as 0.964.

Figure 20 presents the measured and predicted results in terms of effective stress path, the relationship between deviator stress and axial strain. The test results indicate that the clay appears softer when the strain rate is lower. This is mainly because a decrease in the deviatoric strain rate in-

Table 1 Parameters for clays

Clay types	Parameters						
	M	λ	κ	v	ψ	χ	$\bar{e}_0$ [a)]
Wenzhou clay	1.230	0.384	0.042	0.25	0.03	20	2.677
SFBM	1.400	0.370	0.054	0.2	0.009	20	3.544
HKMD	1.265	0.200	0.044	0.3	0.0046	2	0.964

a) $\bar{e}_0$ corresponds to the initial consolidation pressure p_0=10, 78.5 and 400 kPa for Wenzhou clay, SFBM and HKMD, respectively.

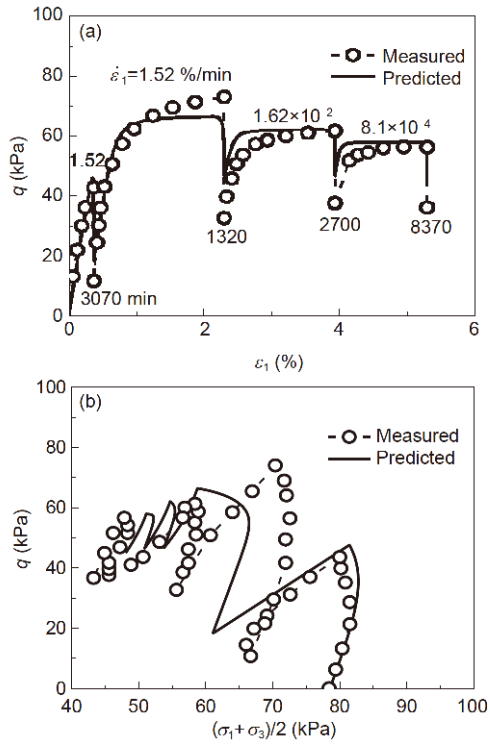

Figure 19 Comparisons between measured and predicted results for undrained triaxial compression test at step-changed axial strain rate. (a) Deviator stress q versus axial strain ε_1; (b) deviator stress q versus stress $(\sigma_1+\sigma_3)/2$.

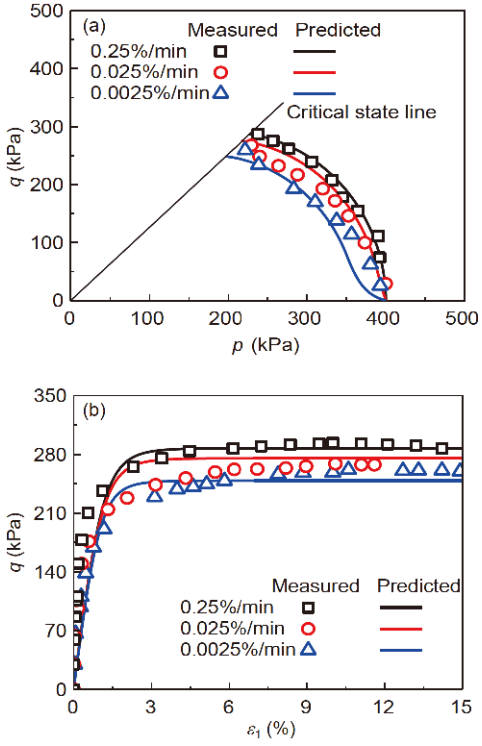

Figure 20 (Color online) Comparison between measured and predicted results for undrained triaxial compression tests at constant strain rate. (a) Deviator stress q versus mean effective stress p; (b) deviator stress q versus axial strain ε_1.

creases the time to produce viscous deformation in the loading process, and thus decreases the proportion of the elastic-plastic deformation produced by stress. Comparisons between measured and predicted results indicate that the EMCC model adequately reflect the strain rate effects of remoulded HKMD under undrained conditions.

3.5.4 *Undrained triaxial stress relaxation tests*

Zhu [6] provided data of undrained stress relaxation tests on remoulded HKMD. The specimens were first loaded at constant strain rate $\dot{\varepsilon}_1$ to a given axial strain ε_1. Then, the axial strains were kept constant and stress relaxation processes were started. The details of two stress relaxation tests are presented in Table 2, where p_0 is the consolidation pressure before shearing. The initial OCR is taken as 1.1 to consider the consolidation time before shearing.

Figure 21 illustrates the relationship between deviator stress ratio q/q_0 and the elapsed time immediately after the starting of the stress relaxation. Here, q_0 is the deviator stress at the beginning of the relaxation process. The test results indicate that the higher the axial strain rate before stress relaxation is, the larger the decay of the deviator stress will be. The EMCC model reasonably reproduces the undrained stress relaxation processes of remoulded HKMD, as indicated by the comparisons between measured and predicted results.

Table 2 Details of the undrained stress relaxation tests

Test number	p_0 (kPa)	ε_1 (%)	$\dot{\varepsilon}_1$ (%/min)
CUC1	200	7.3	0.001
CUC5	400	17.1	0.025

3.5.5 *Undrained triaxial creep tests*

Zhu [6] conducted three undrained creep tests on remoulded HKMD. The consolidation pressure was 400 kPa. The specimens were fast loaded under the undrained triaxial compression conditions until the deviator stresses reach 134, 189 and 243 kPa, respectively. Subsequently, the total stress was kept constant in the following creep process. The initial OCR was determined as 1.15 by fitting the undrained creep tests data.

Figure 22 shows the changes of axial strain and pore water pressure with creep time. As indicated by Figure 22(a), when the deviator stress level is low, the axial strain develops in a decreasing rate. When the deviator stress level is high, the axial strain rate gradually increase, which reflects the acceleration creep [15,28,32]. Although some deviations are observed, comparisons between measured and predicted results indicate that the EMCC model captures undrained acceleration creep behaviour of remoulded HKMD at high deviator stress levels.

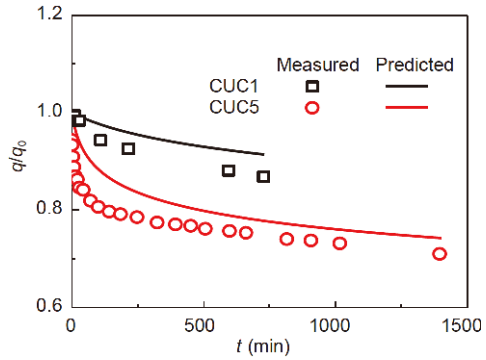

Figure 21 (Color online) Comparison between measured and predicted results for undrained triaxial stress relaxation tests.

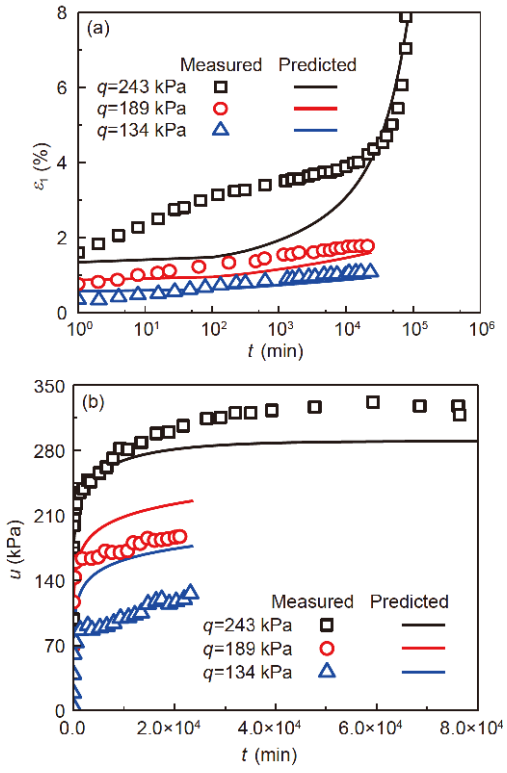

Figure 22 (Color online) Comparison between measured and predicted results for undrained triaxial creep tests. (a) Axial strain ε_1 versus creep time; (b) pore water pressure u versus creep time.

4 Conclusions

A new method to develop EP models into EPV models for clays was proposed. The elastic-plastic strain increments were obtained by simple improvements in existing EP models. The novel RSL concept was proposed to determine OCR, and the OCR was introduced into the viscous flow rule to calculate the viscous strain increment. The influences of stress and time on evolution of the yield surface were separated, thus making the loading-unloading criterion extremely simple and comparable to that of EP models. The proposed method can be applied in principle to any existing EP model for clays. In addition, the time-dependent behaviours of clays under isotropic compression conditions were schematically presented.

Based on the proposed method, the MCC model was extended into the EMCC model. Comparisons between measured and predicted results indicate that the EMCC model adequately captures time-dependent behaviours of clays, such as creep, stress relaxation and strain rate effects. In particular, it can also describe acceleration creep under undrained conditions.

Appendix

Deviation of $\mathrm{d}\varepsilon_{\mathrm{v}}^{\mathrm{s}}$ under isotropic compression conditions

The void ratio increment of clays under the normal consolidation state is derived by differentiating eq. (12).

$$\mathrm{d}e = -\lambda\frac{\mathrm{d}p}{p}. \tag{a1}$$

Substituting eq. (a1) into eq. (18) in conjunction with the initial void ratio $\bar{e}_0$, the instant volumetric strain is derived as

$$\mathrm{d}\bar{\varepsilon}_{\mathrm{v}}^{\mathrm{s}} = \frac{\lambda}{1+\bar{e}_0}\frac{\mathrm{d}p}{p}. \tag{a2}$$

The slope of instant swelling line in the e-ln$p$ plane is κ, and thus the elastic volumetric strain increment is expressed as

$$\mathrm{d}\bar{\varepsilon}_{\mathrm{v}}^{\mathrm{e}} = \frac{\kappa}{1+\bar{e}_0}\frac{\mathrm{d}p}{p}. \tag{a3}$$

Substituting eqs. (a2) and (a3) into eq. (2) gives the instant plastic volumetric strain increment.

$$\mathrm{d}\bar{\varepsilon}_{\mathrm{v}}^{\mathrm{p}} = \frac{\lambda-\kappa}{1+\bar{e}_0}\frac{\mathrm{d}p}{p}. \tag{a4}$$

Substituting eq. (a4) into eq. (5), the instant plastic volumetric strain for clays under the overconsolidation state can be expressed as

$$\mathrm{d}\varepsilon_{\mathrm{v}}^{\mathrm{p}} = \xi_{\mathrm{iso}}\frac{\lambda-\kappa}{1+\bar{e}_0}\frac{\mathrm{d}p}{p}, \tag{a5}$$

where ξ_{iso} denotes the value of ξ under isotropic compression conditions.

The elastic volumetric strain increment is written as

$$\mathrm{d}\varepsilon_{\mathrm{v}}^{\mathrm{e}} = \frac{\kappa}{1+e_0}\frac{\mathrm{d}p}{p}. \tag{a6}$$

Substituting eq. (a5) and (a6) into eq. (2), the instant volumetric strain increment under isotropic compression conditions is obtained.

$$\mathrm{d}\varepsilon_{\mathrm{v}}^{\mathrm{s}} = \frac{\kappa}{1+e_0}\frac{\mathrm{d}p}{p} + \xi_{\mathrm{iso}}\frac{\lambda-\kappa}{1+\bar{e}_0}\frac{\mathrm{d}p}{p}. \tag{a7}$$

This work was supported by the National Natural Science Foundation of China (Grant Nos. 51522802, 51778026, 51421005 & 51538001) and the Natural Science Foundation of Beijing (Grant No. 8161001).

1 Liingaard M, Augustesen A, Lade P V. Characterization of models for time-dependent behavior of soils. Int J Geomech, 2004, 4: 157–177
2 Sivasithamparam N, Karstunen M, Bonnier P. Modelling creep behaviour of anisotropic soft soils. Comput Geotech, 2015, 69: 46–57
3 Feng W Q, Lalit B, Yin Z Y, et al. Long-term non-linear creep and swelling behavior of Hong Kong marine deposits in oedometer condition. Comput Geotech, 2017, 84: 1–15
4 Wang Z, Wong R C K. Strain-dependent and stress-dependent creep model for a till subject to triaxial compression. Int J Geomech, 2016, 16: 04015084
5 Yin Z Y, Zhu Q Y, Zhang D M. Comparison of two creep degradation modeling approaches for soft structured soils. Acta Geotech, 2017, 12: 1395–1413
6 Zhu J G. Experimental study and elastic visco-plastic modelling of the time dependent behavior of Hong Kong marine deposits. Dissertation of Doctoral Degree. Hong Kong: Hong Kong Polytechnic University, 2000
7 Li D W, Fan J H, Wang R H. Research on visco-elastic-plastic creep model of artificially frozen soil under high confining pressures. Cold Regions Sci Tech, 2011, 65: 219–225
8 Madaschi A, Gajo A. A one-dimensional viscoelastic and viscoplastic constitutive approach to modeling the delayed behavior of clay and organic soils. Acta Geotech, 2017, 12: 827–847
9 Zhou H W, Wang C P, Han B B, et al. A creep constitutive model for salt rock based on fractional derivatives. Int J Rock Mech Min Sci, 2011, 48: 116–121
10 Desai C S, Sane S, Jenson J. Constitutive modeling including creep- and rate-dependent behavior and testing of glacial tills for prediction of motion of glaciers. Int J Geomech, 2011, 11: 465–476
11 Kong Y, Xu M, Song E. An elastic-viscoplastic double-yield-surface model for coarse-grained soils considering particle breakage. Comput Geotech, 2017, 85: 59–70
12 Yin Z Y, Karstunen M, Chang C S, et al. Modeling time-dependent behavior of soft sensitive clay. J Geotech Geoenviron Eng, 2011, 137: 1103–1113
13 Wang S, Wu W, Yin Z Y, et al. Modelling the time-dependent behaviour of granular material with hypoplasticity. Int J Numer Anal Methods Geomech, 2018, 42: 1331–1345
14 Yang C, Carter J P, Sheng D, et al. An isotach elastoplastic constitutive model for natural soft clays. Comput Geotech, 2016, 77: 134–155
15 Yao Y P, Kong L M, Zhou A N, et al. Time-dependent unified hardening model: Three-dimensional elastoviscoplastic constitutive model for clays. J Eng Mech, 2015, 141: 04014162
16 Yao Y P, Kong L M, Hu J. An elastic-viscous-plastic model for overconsolidated clays. Sci China Tech Sci, 2013, 56: 441–457
17 Yin Z Y, Xu Q, Yu C. Elastic-viscoplastic modeling for natural soft clays considering nonlinear creep. Int J Geomech, 2015, 15: A6014001
18 Tong X, Tuan C Y. Viscoplastic cap model for soils under high strain rate loading. J Geotech Geoenviron Eng, 2007, 133: 206–214
19 Cassiani G, Brovelli A, Hueckel T. A strain-rate-dependent modified Cam-Clay model for the simulation of soil/rock compaction. Geomech Energy Environ, 2017, 11: 42–51
20 Adachi T, Oka F, Mimura M. Mathematical structure of an overstress elasto-viscoplastic model for clay. Soils Found, 1987, 27: 31–42
21 Yin Z Y, Hicher P Y. Identifying parameters controlling soil delayed behaviour from laboratory and *in situ* pressuremeter testing. Int J Numer Anal Meth Geomech, 2008, 32: 1515–1535
22 Rowe R K, Hinchberger S D. The significance of rate effects in modelling the Sackville test embankment. Can Geotech J, 1998, 35: 500–516
23 Perzyna P. Fundamental problems in viscoplasticity. Adv Appl Mech, 1966, 9: 243–377
24 Perzyna P. The constitutive equations for rate sensitive plastic materials. Quart Appl Math, 1963, 20: 321–332
25 Hinchberger S D, Rowe R K. Modelling the rate-sensitive characteristics of the Gloucester foundation soil. Can Geotech J, 1998, 35: 769–789
26 Islam M N, Gnanendran C T. Elastic-viscoplastic model for clays: Development, validation, and application. J Eng Mech, 2017, 143: 04017121
27 Kutter B L, Sathialingam N. Elastic-viscoplastic modelling of the rate-dependent behaviour of clays. Géotechnique, 1992, 42: 427–441
28 Qiao Y, Ferrari A, Laloui L, et al. Nonstationary flow surface theory for modeling the viscoplastic behaviors of soils. Comput Geotech, 2016, 76: 105–119
29 Katona M G. Evaluation of viscoplastic cap model. J Geotech Eng, 1984, 110: 1106–1125
30 Sekiguchi H. Theory of undrained creep rupture of normally consolidated clay based on elasto-viscoplasticity. Soils Found, 1984, 24: 129–147
31 Yin J H, Graham J. Elastic viscoplastic modelling of the time-dependent stress-strain behaviour of soils. Can Geotech J, 1999, 36: 736–745
32 Yin J H, Zhu J G, Graham J. A new elastic viscoplastic model for time-dependent behaviour of normally and overconsolidated clays: Theory and verification. Can Geotech J, 2002, 39: 157–173
33 Bjerrum L. Engineering geology of Norwegian normally-consolidated marine clays as related to settlements of building. Géotechnique, 1967, 17: 83–118
34 Xiao Y, Liu H L, Liu H, et al. Unified plastic modulus in the bounding surface plasticity model. Sci China Tech Sci, 2016, 59: 932–940
35 Dafalias Y F. Bounding surface plasticity. I: Mathematical foundation and hypoplasticity. J Eng Mech, 1986, 112: 966–987
36 Yao Y P, Hou W, Zhou A N. UH model: Three-dimensional unified hardening model for overconsolidated clays. Géotechnique, 2009, 59: 451–469
37 Bodas Freitas T M, Potts D M, Zdravkovic L. Implications of the definition of the Φ function in elastic-viscoplastic models. Géotechnique, 2012, 62: 643–648
38 Kelln C, Sharma J, Hughes D, et al. An improved elastic-viscoplastic soil model. Can Geotech J, 2008, 45: 1356–1376
39 Leoni M, Karstunen M, Vermeer P A. Anisotropic creep model for soft soils. Géotechnique, 2008, 58: 215–226
40 Yin Z Y, Chang C S, Karstunen M, et al. An anisotropic elastic-viscoplastic model for soft clays. Int J Solids Struct, 2010, 47: 665–677
41 Wang L Z, Dan H B, Li L L. Modeling strain-rate dependent behavior of KR_0-consolidated soft clays. J Eng Mech, 2012, 138: 738–748
42 Yin Z Y, Zhu Q Y, Yin J H, et al. Stress relaxation coefficient and formulation for soft soils. Géotech Lett, 2014, 4: 45–51
43 Kongkitkul W, Kawabe S, Tatsuoka F, et al. A simple pneumatic loading system controlling stress and strain rates for one-dimensional compression of clay. Soils Found, 2011, 51: 11–30
44 Nash D F T, Sills G C, Davison L R. One-dimensional consolidation testing of soft clay from Bothkennar. Géotechnique, 1992, 42: 241–256
45 Zhang X, Lytton R L. Modified state-surface approach to the study of unsaturated soil behavior. Part III: Modeling of coupled hydro-mechanical effect. Can Geotech J, 2012, 49: 98–120
46 Lu D, Ma C, Du X, et al. Development of a new nonlinear unified strength theory for geomaterials based on the characteristic stress concept. Int J Geomech, 2017, 17: 04016058
47 Ma C, Lu D, Du X, et al. Developing a 3D elastoplastic constitutive model for soils: A new approach based on characteristic stress. Comput Geotech, 2017, 86: 129–140
48 Voyiadjis G Z, Song C R. Finite strain, anisotropic modified cam clay model with plastic spin. I: Theory. J Eng Mech, 2000, 126: 1012–1019

49 Yin Z Y, Jin Y F, Shen J S, et al. Optimization techniques for identifying soil parameters in geotechnical engineering: Comparative study and enhancement. Int J Numer Anal Methods Geomech, 2018, 42: 70–94
50 Jin Y F, Yin Z Y, Zhou W H, et al. A single-objective EPR based model for creep index of soft clays considering L_2 regularization. Eng Geol, 2019, 248: 242–255
51 Yin Z Y, Jin Y F, Shen S L, et al. An efficient optimization method for identifying parameters of soft structured clay by an enhanced genetic algorithm and elastic-viscoplastic model. Acta Geotech, 2017, 12: 849–867
52 Yin Z Y, Yin J H, Huang H W. Rate-dependent and long-term yield stress and strength of soft Wenzhou marine clay: Experiments and modeling. Mar Georesources Geotech, 2015, 33: 79–91
53 Lacerda W A. Stress-relaxation and creep effects on soil deformation. Dissertation of Doctoral Degree. Berkeley: University of California, 1976
54 Jiang J, Ling H I, Kaliakin V N, et al. Evaluation of an anisotropic elastoplastic-viscoplastic bounding surface model for clays. Acta Geotech, 2017, 12: 335–348